Mechanical Characterization of the Human Pia-Arachnoid Complex

Nikolaus Benko[1] MS, Emma Luke[2] BS, Yousef Alsanea[1] BS, Brittany Coats[1] PhD

[1] Department of Mechanical Engineering
University of Utah
Salt Lake City, UT
USA

[2] Department of Biomedical Engineering
University of Rochester
Rochester, NY
USA

Corresponding Author:

Brittany Coats
University of Utah
1495 E 100 S (1550 MEK)
Salt Lake City, UT 84112
USA
Email: brittany.coats@utah.edu

Abstract

Traumatic brain injury (TBI) is a significant problem in global health that affects a wide variety of patients. Mild forms of TBI such as axonal injury, commonly referred to as concussion, are a result of rapid accelerations of the head from either direct or indirect impacts. Kinetic energy from the impact is transferred into deformation of the brain, leading to cellular disruption. This transfer of energy is in part mediated by the pia-arachnoid complex (PAC), a layer of anatomical structures that forms the physical connection between the brain and the skull. The importance of properly quantifying the mechanics of the PAC for use in computational models of TBI has been understood for some time, but data from human subjects has been unavailable. In this study, we quantify the normal traction modulus of the PAC in five post-mortem human subjects using hydrostatic fluid pressurization in combination with optical coherence tomography. Testing at multiple locations across each brain reveals that brain-skull stiffness is heterogeneously distributed. The material response to traction loading was linear, with a mean normal traction modulus of 12.6±4.8 kPa. Modulus was 21% greater in superior regions of the brain compared to inferior regions. Comparisons with regional microstructural data suggests a potential relationship between the volume fraction of arachnoid trabeculae and modulus. Comparisons to coincident measurements of microstructural properties showed a positive correlation between arachnoid membrane thickness and normal traction modulus. This study is the first to characterize the mechanics of the human pia-arachnoid complex and quantify material properties *in situ.* These findings suggest implementing a heterogeneous model of the brain-skull interface in computational models of TBI may lead to more realistic injury prediction.

Keywords- **Pia-Arachnoid Complex**, **Traumatic Brain Injury, Brain-Skull Interface, Optical Coherence Tomography**

Introduction

Traumatic brain injury (TBI) is a significant global health problem with millions of instances of TBI in the United States each year and many more worldwide (Langlois, Rutland-Brown and Wald, 2006; Coronado *et al.*, 2012). TBI is commonly caused by direct impact to the head from falls or collisions, resulting in rapid head acceleration or deceleration. Computational modeling has become an important tool for studying the biomechanics of TBI, relating the conditions of head impact to physical deformations of brain tissues. Model accuracy depends on the adequate characterization of brain materials as well as surrounding bone and soft tissue (Zhao, Choate and Ji, 2018). Numerous studies have characterized the material properties of the skull, the dura mater, cortical grey and white matter, but few efforts have focused on the human pia-arachnoid complex (PAC), which connects the brain to the skull and plays a role in constraining brain deformation during injury (Cloots *et al.*, 2008, 2011, 2013; Cloots, van Dommelen and Geers, 2012; Alhilali *et al.*, 2015; Ji *et al.*, 2015).

The PAC, often referred to as the leptomeninges, or just the meninges in some modeling contexts, is defined as the anatomical region between the arachnoid mater, and the pia mater. The superficial side of the arachnoid mater is adhered to the deep side of the dura mater via arachnoid border cells, while the superficial side of the dura is adhered to the interior of the skull. The space between the deep side of the arachnoid mater and the superficial pia mater is filled with cerebral spinal fluid and spanned by arachnoid trabeculae and subarachnoid vasculature. The pia mater sits directly on top of cortical grey matter, thus the primary mechanical connection that supports tensile and shear loading between the cerebrum and the skull are formed by the arachnoid trabeculae and subarachnoid vasculature (Haines, 1991; Haines and Ard, 2002).

To date, most computational models of TBI assume either solid linear elastic homogeneous behavior of the PAC or a fluid like behavior based on the properties of cerebral spinal fluid within the subarachnoid space (Mao *et al.*, 2013; Patton, McIntosh and Kleiven, 2013; Ji *et al.*, 2015). The accuracy of these two methods is highly dependent on the load configuration at any given time point. For example, the solid model can be calibrated to properly represent the tethering properties of the arachnoid trabeculae

in tension, but it will not reflect the likely buckling of these structures under compression, and ignores the support of incompressible cerebral spinal fluid. On the other hand, a fluid-based model ignores the tensile and shear support of the arachnoid trabeculae. Further, all current models assume homogeneous material properties. These assumptions of mechanical behavior have yet to be confirmed by experimental measurements of the human PAC, despite knowledge that the PAC significantly affects estimates of brain strain and injury prediction (Kuijpers, Claessens and Sauren, 1995; Saboori and Sadegh, 2011; Ghaffari *et al.*, 2014; Scott, Margulies and Coats, 2016; De Kegel *et al.*, 2018; Zhao, Wei; Stemper and Ji, 2019; Zhou, Li and Kleiven, 2019). In order to improve state-of-the-art models of TBI, biofidelic mechanical models of the PAC are required.

The size of the structures in the PAC is small, on the order of tens of micrometers, in comparison to the size of the brain and other common components included in TBI finite element models. Because of this small size, explicit modeling of constituent components of the PAC within a larger TBI model is not computationally feasible. Thus, studies of PAC mechanical properties have focused on macroscopic responses of the PAC. Scott et. al utilized a multiscale approach to estimate macroscale behavior of the PAC based on estimates of the amounts of arachnoid trabeculae and subarachnoid vasculature in microscale models of piglet PAC (Scott, Margulies and Coats, 2016). This method improved predictions of extra axial hemorrhage; however, the material response of the PAC was estimated based on animal data in the literature (Scott and Coats, 2015; Scott, Margulies and Coats, 2016). Jin et. al. measured macroscopic material properties of bovine PAC using *ex vivo* traction and shear tests. Their tests were used to determine a transversely isotropic constitutive model, but no data exists to translate between bovine and human material properties. Additionally, the effect of tissue removal and test preparation were not studied (Jin *et al.*, 2006, 2014; Jin, Yang and King, 2011). Yin et al. used magnetic resonance elastography to measure the relative displacement between the brain and skull resulting from small 60 Hz vibrations. They reported that relative displacement was not homogeneously distributed across the brain-skull interface (Yin *et al.*, 2018). Most recently, Fabris, Suar, and Kurt, measured localized variations in elastic response of the rat PAC using atomic force microscopy and demonstrated a correlation between

local material properties and protein content indicative of collagen structures(Fabris, Suar and Kurt, 2019). To date, no experimentally measured material properties of the human PAC exist.

The objective of this study was to quantify the normal traction modulus of the human PAC and assess its regional variability. To achieve this objective, we imaged the human pia-arachnoid complex via optical coherence tomography (OCT) and conducted *in situ* mechanical testing of the PAC in traction through fluid pressurization of the subarachnoid space. Regional modulus data were compared to qualitative metrics of microstructure content to identify relationships between microstructural features and material response. This study provides valuable human material property data for use in computational modeling of TBI. It also provides insight into the relationship between PAC microstructure and material properties, and identifies that a heterogeneous material variation of the PAC that may be necessary for biofidelic computational modeling of human TBI.

Methods

Post-Mortem Human Subject Head Preparation

Studies were reviewed by the University of Utah Institutional Review Board and determined to be exempt from human study regulation. Human cadavers were selected as the subjects of the study because material properties of the brain and skull are typically species-dependent (Prange and Meaney, 2000; Coats and Margulies, 2006; Margulies and Coats, 2013). Fresh-frozen human cadaver heads (Table 1, ages 32-86 years old, n=5, purchased from Science Care Inc. Phoenix, Arizona USA) were defrosted over 2 days in a refrigerator in an upright position and then allowed to reach room temperature over 8 hours. The causes of death include prostate cancer, gastric cancer, cardiopulmonary arrest, cardiovascular disease, and acute interstitial pneumonitis. A craniotomy was performed on each hemisphere of the skull to open a 15cm (frontal-occipital direction) by 7cm (inferior-superior direction) using an autopsy saw (model Shandon 10000, Thermo Fisher Scientific, Waltham Massachusetts). The sagittal sinus was left intact to keep the cerebrum in place. Dura between the sagittal sinus and temple region was removed, exposing the PAC. Heads were placed upright in a custom stereotactic frame for OCT imaging.

Inflation Procedure

In each location, a 27-gauge needle was inserted through the arachnoid membrane near the junction of two or more sulci (Fig. 1A). In these locations, the depressurized arachnoid membrane spanned the gyrus and left a defined subarachnoid space. The subarachnoid space was inflated to physiological intracranial pressure (10±1.5 mmHg) using a custom feedback-controlled manometer (Fig. 1B) consisting of a pressure monitor (Pendotech, model 1-06-64-04-2), a syringe pump (NE-300 New Era Pump Systems) and a 90 cm tall fluid reservoir. Feedback control was provided by an Arduino Uno (Arduino AD) and MATLAB (Mathworks) program. Saline was pumped into the manometer reservoir at a rate of 10 mL per minute until the baseline 10 mmHg pressure was reached. Inflation was then paused; a volumetric scan was taken with the OCT and then video recording was started. The pressure was then increased linearly to 30 mmHg over the course of 100 seconds by continuously adding fluid to the manometer. An example of the time-series inflation resulting from this procedure is shown in Fig. 2.

Imaging Protocol

OCT imaging was conducted with a Bioptigen R2200 spectral OCT scanner (Leica Microsystems Inc. Buffalo Grove, Illinois USA) and a 12 mm telecentric lens. Scan volume was set to 5 mm x 5 mm x 1.64 mm with 800 A-scans per B-scan, 400 B-scans, and a single C-scan. The axial resolution of the system was 1.6 μm, the lateral resolution was 6.25 μm, and depth resolution was 12.5 μm (Fig 1C). Screen recording software (Apowersoft Screen Recorder Pro, Apowersoft Limited, Hong Kong) was used to capture videos of inflation tests at 24 frames per second. Between 8 and 12 locations were inflated and imaged for each hemisphere of each brain. Each hemisphere was subdivided into a 2x3 grid to classify regions as frontal, parietal, or occipital and as inferior or superior for a total of 12 regions per brain.

Image Processing and Strain Measurement

A post hoc video analysis script tracked the displacement of the arachnoid membrane throughout the inflation process. Briefly, an initial mask was generated by a user-defined trace of the arachnoid membrane on the first frame of the video recording. Subsequent movement of the membrane was detected using a Sobel edge finding algorithm. A cubic spline was fit to the membrane edge, and the displacement

of the membrane was defined as the average change in height of the spline. Displacement data were synchronized with pressure data and converted to engineering strain by assuming a 1 mm initial distance between the arachnoid membrane and pia mater. This distance was chosen based on our estimate of average distance between the arachnoid membrane and pia across the width of the sulci used for testing. Stress was defined as the hydrostatic pressure measured by the manometer. The stress-strain response was linear in the loading range of 10-30 mmHg. Therefore, linear regression was used to estimate normal traction modulus at each location. This normal traction modulus is an 'effective' modulus for the entire volume being imaged and not a true material modulus for the individual structures in the volume. OCT videos were recorded in two intersecting perpendicular planes centered near the midpoint of the imaging volume. The normal traction modulus calculated in each plane were averaged to determine the effective normal traction modulus for a given location. During initial review of inflation videos, it was noted that some image locations consisted of trabecular fibers unfolding, like an accordion, rather than stretching. Therefore, all inflation videos were reviewed and tests categorized as either purely unfolding, purely tensile loading of trabeculae, or a combination of the two regimes.

Correlations between normal traction modulus and subject age, sex, and post-mortem cadaver acquisition time were evaluated using a linear mixed model with age, sex, and post-mortem procurement time as fixed effects. Subject ID with unequal variances was used to represent the repeated measures structure of our studies in the linear mixed model. Statistical analyses were performed in JMP Pro 14 (SAS Institute Inc. Cary, North Carolina USA). A one-way Analysis of Variance (ANOVA) with repeated measures was used to determine the effect of brain region on normal traction modulus. An ANOVA was also used to evaluate differences in normal traction modulus between subjects. *P*-values less than 0.05 were considered statistically significant.

Correlations with PAC Microstructure

To draw connections between the local material properties and microstructural components of the PAC, modulus data were compared with arachnoid trabeculae volume fraction (ATVF), arachnoid membrane thickness (AMT), and subarachnoid vasculature volume fraction (VVF) extracted from the

OCT images. ATVF is a measurement of the volume fraction of segmented trabeculae from the PAC and was reported previously by our group. Briefly, for each imaging volume, three 2D images were selected from the image stack for analysis. One image represented the middle of the image stack. The other two images were located at approximate mid-points between the center image and the endpoints of the image stack. In each image, trabeculae were segmented and the number of segmented pixels relative to the total number of pixels was calculated. The area fractions across all three images were averaged to represent a 'volume fraction'. We have previously shown that this approach results in a good approximation of 3D volume fraction (Scott and Coats, 2015). The same methodology was used to estimate VVF. AMT was calculated by measuring and averaging thickness in 3 locations on the 3 images slices. Each of these measurements (ATVF, VVF, and AMT) were made at coincident locations to the *in situ* pressurization. Bivariate and multivariate correlations between coincident measurements of normal traction modulus and microstructural metrics were evaluated in JMP Pro 14.

Results

Elastic response was measured at 109 locations throughout the 5 subjects. Membrane tracking algorithms failed to properly track membrane displacement in 21 locations. This was largely due to tortuous membrane surfaces which did not produce reliable features for tracking or rapid movement of the OCT lens during acquisition. These data were excluded, leaving 88 successful measurements for analysis. Mean normal traction modulus ± standard deviation across all measurements was 10.7±5.1 kPa. The average ± standard deviation of the coefficient of determination (R^2) for the linear regressions used to extract the traction modulus was 0.965±0.107. The median value as 0.992. The average difference between the modulus measurements from the perpendicular view at each location was 1.31 kPa. The lowest modulus measured was 2.39 kPa and the highest measured was 22.5 kPa. Normal traction modulus was significantly different between loading regimes, with fully loaded trabeculae having the highest modulus (12.6±4.8 kPa, p=0.0007) and unfolding trabeculae having the lowest modulus (8.06±4.3 kPa). Tests showing a combination of the two regimes had a modulus of 8.93±3.3 kPa. An example of the

stress-strain response in these three regimes from a single subject is provided in Figure 3. Because of these differences, we focused our remaining analysis only on the fully recruited trabeculae, as this gives the best estimate of the PAC substructures in tension. The stress-strain data from the fully recruited trabeculae across all 5 subjects are provided in Figure 4. To ensure that the omission of tests involving unfolding trabeculae would not bias regional analyses, a Chi Squared test was used to test for correlation between inflation regime and region. Neither superior-inferior grouping (p=0.327) or frontal-parietal-occipital groupings had any correlation with inflation regime (p=0.472). The dataset was further restricted by removing tests in which fibers were detached from the cortical surface (n=4).

There were no significant differences between left (12.13±5.3 kPa) and right (13.07±4.4 kPa) hemispheres (Table 2). Normal traction modulus was significantly higher in superior regions (12.9±4.9 kPa) with mean moduli 21% greater than inferior regions (10.4±4.2 kPa, p=0.0224). Frontal (11.1±4.53 kPa), parietal (11.3±4.61 kPa), and occipital (13.8±4.7 kPa) regions displayed no significant differences (p=0.36).

Female subjects (n=2, Subjects 4 and 5) had a 24% higher average modulus (14.7±4.04 kPa) compared to male subjects (11.6±4.84 kPa, n=3, Fig. 5). However, this finding is confounded by a negative trend between modulus and time between subject death and freezing. Female subjects had procurement times of 4 and 6 days, while male subjects had procurement times of 9 and 11 days. Results of the linear mixed model with repeated measures found that sex (p=0.42), age (p=0.55), and post mortem cadaver procurement time (p=0.26), did not have statistically significant effects on modulus measurements. However, these analyses likely had low power due to the limited sample size.

Material property data were also compared with the microstructural data previously published by our lab and additional new characterization of arachnoid membrane thickness and volume fraction of subarachnoid vasculature (Fig. 6). Subarachnoid vascular volume fraction (VVF) ranged between 0, indicating no vessels present, and 0.278 with a mean and standard deviation of 0.069±0.075. The distribution of VVF was heavily skewed towards 0 with only a few locations containing large amounts of vasculature. Because of this skew, a non-parametric Wilcoxon signed-rank test was used to evaluate

regional differences in VVF. VVF was significantly higher in parietal regions (0.092±0.087) when compared to frontal regions (0.025±0.031 p=0.018) and occipital regions (0.074±0.068, p=0.021). No other regional trends in VVF were observed. Arachnoid membrane thickness (AMT) ranged from 20.0 μm to 53.3 μm with a mean and standard deviation of 37.6±8.2 μm. No regional trends in AMT were observed. However, AMT decreased with increased time between death and freezing, similar to modulus. Bivariate correlation analysis of coincident measurements revealed no significant correlations between microstructural measurements of ATVF (r=0.01, p=0.64) or VVF (r=0.004, p=0.70). Modulus was significantly correlated with AMT (r=0.121, p=0.024). Second order multivariate analysis showed no significant effects ATVF, VVF, and AMT (r=0.215, p=0.1763).

To better view the heterogeneity of the traction modulus across the surface of the brain, a spatial map was created using Voronoi tessellation. Voronoi tessellation creates a collection of polygon cells by constructing perpendicular bisectors between seed points. The coordinates for each imaging location across all subjects were used for the seed points in the spatial map. A grayscale value between 0 and 1 was then assigned to each Voronoi cell based on the average volume fraction measured at that imaging location. A colormap was assigned to map grayscale values to a RGB color triplet. The resulting spatial map (Fig. 7) highlights the findings from the ANOVAs. Specifically, that inferior and frontal regions of the brain generally have lower traction moduli than superior and occipital regions of the brain.

Discussion

In this study, mechanical testing of human cadaver PAC was performed via fluid pressurization. Controlled inflation of the sub-arachnoid space effectively placed trabecular fibers in tension. Deformation tracking via optical coherence tomography and post-hoc video analysis revealed a linear elastic material response in traction. This finding corresponds with results from an *ex vivo* test of bovine PAC in normal traction, and computational estimates of human and porcine PAC stiffness (Jin *et al.*, 2007; Saboori and Sadegh, 2011; Scott, Margulies and Coats, 2016). The overall average measured

modulus of 12.7 kPa is between the 61 kPa reported for bovine PAC by Jin et al. (2007) and 1 kPa suggested by the modeling approach of Saboori and Sadegh (2011). Variances between the values likely stem from species differences, testing methods, and assumptions of computational models.

Finite element models of the human head have represented the PAC with the same variability as the above referenced experimental data. The KTH human head model (Kleiven, 2006) represents the PAC with an elastic modulus of 126 kPa, 10 times our reported value. The SIMon head model (Takhounts *et al.*, 2008) and ICLHM head model (Ghajari *et al.*, 2019) both utilize 60 kPa, which is similar to the bovine PAC measurements reported by Jin et al. (2007). The only model that utilizes a lower PAC elastic modulus is the GHBMC head model (Mao *et al.*, 2013) which uses 1.5 kPa. Our measured average modulus was 12.5 kPa (range: 5-24 kPa). This may mean that the models utilizing stiffer PAC elastic moduli may be underestimating brain-skull displacement and brain strain. However, any underestimation from a stiffer PAC may be mediated somewhat by compensatory brain properties. For example, the SIMon head model which has an estimated PAC elastic modulus of 60 kPa utilizes soft brain material properties while the GHBMC head model, which has an estimated PAC modulus of 1.5 kPa, has stiffer brain material properties. Nearly all head finite element models have been tuned to some degree to match validation data and also have varying internal brain structures and properties that similarly effect the overall mechanical response of the brain.

Regardless of the value used to represent the PAC, all finite element head models represent the PAC with uniform properties across the surface of the brain. We evaluated the mechanics of the PAC at multiple locations across the brain and revealed that PAC traction stiffness is regionally dependent with increased modulus in superior regions. Our Voronoi tessellation map highlights the PAC heterogeneity across the brain and the stiffer PAC in superior regions (Fig. 7). We saw a trend of increasing stiffness near the occipital region of the brain, but large variability precluded statistical significance. It should be noted that our regions were defined using a grid system, and perhaps stronger trends would be seen if they were defined using cortical lobe definitions. In conjunction with findings from Scott et al. (2016), Yin et al. (2018), and Fabris et al. (2019), our data suggest that a heterogeneous material description of the PAC

may be more appropriate for computational modeling of human TBI (Scott, Margulies and Coats, 2016; Yin *et al.*, 2018; Fabris, Suar and Kurt, 2019).

Correlations between modulus and coincident measurements of ATVF, VVF, and AMT produced mixed results. Quantitative metrics characterizing the relative amounts of trabecular fibers and subarachnoid vessels, the two structures that tether the arachnoid mater to the pia, did not correlate with modulus. Increased VVF in parietal regions, which are likely due to the presence of large vessels such as the middle cerebral artery that supply the parietal and temporal lobes, did not correspond with increases in modulus in the same areas, suggesting vessels do not play a significant role in PAC response to traction loads. This finding seems logical for the regions imaged in our study as most vessels we observed ran parallel to the arachnoid membrane. Imaging closer to the sagittal sinus, where vessels are more perpendicular to the PAC, may have different correlations.

Arachnoid membrane thickness significantly correlated with normal traction modulus. However, a relatively low Pearson correlation coefficient value of 0.215 indicates this is not a consistent effect. One possible explanation for the correlation between AMT and modulus is that increased membrane thickness creates increased resistance to bending of the arachnoid membrane during inflation. As the PAC is pressurized, the arachnoid membrane remains in contact with cortical gyri at the edge of the inflation region. This significant correlation, however is confounded by the fact that both AMT and modulus decreased with increased time between subject death and tissue freezing. More research needs to be done to identify mechanical changes in both structures with post-mortem time and storage.

Despite coincident data not correlating to the mechanics of the PAC, aggregated regional data suggests a possible link between microstructures constituents of the PAC and macrostructural properties. Prior work from our group found increased volume fraction of arachnoid trabeculae in superior regions of the brain. Likewise, the limited data set presented here shows increased traction stiffness in superior regions (Fig. 5). However, our previous study found higher volume fraction of arachnoid trabeculae in frontal regions of the brain whereas this study finds no significant trends in the anterior-posterior direction. In fact, the average modulus greater in occipital regions. Microstructure metrics included in this

study accounted for the relative density of different anatomical structures, but did not account for microstructure geometry, which likely contributes to the local mechanical response. Future work that considers PAC geometry, such as inverse finite element analysis or digital image correlation, may shed further light on the fundamental connection between PAC microstructure and macrostructure properties. Additional testing to determine PAC response to shear loads would also be beneficial for constructing transversely isotropic material models.

In situ inflation of the PAC demonstrated an effective method of investigating the mechanics of the PAC without excessive chemical interaction with biological materials or removal of neighboring tissue that would be present *in vivo.* However, the study is limited by the yet to be explored effect of freezing and thawing on the mechanics of PAC microstructures. Studies on other collagen-based structures such as tendon and cartilage report no significant alteration to Young's Modulus from freezing and thawing, despite some specimens being frozen up to 30 days (Giannini *et al.,* 2008; Szarko, Muldrew and Bertram, 2010; Lee and Elliott, 2017). This suggests that our measurements may be within the realm of measurements of fresh tissue, but further testing is needed to confirm this hypothesis. An additional limitation of our study was the relatively small sample size due to the difficulty of obtaining post-mortem specimens. Despite these limitations, the techniques developed here are readily applicable to any form of post-mortem subjects and do not require assumptions on the behavior of surrounding tissues as is required with non-contact elastography techniques. Results of this study highlight the mechanical complexity of the subarachnoid space and suggest that the development of heterogeneous material models may aid in the improvement of computational models of TBI.

Conclusion

Mechanical testing of the human PAC using fluid pressurization is a viable method for determining the stiffness of mechanical tethering between the brain and skull. Repeated measurements across the surface of the brain reveal that the strength of tethers is heterogeneous with increased tether stiffness in superior regions. Comparisons with microstructure data highlight the anatomical and mechanical

complexity of the space and the need for further investigation. Based on previous studies by our group and others, incorporating these heterogeneities into computational models of human TBI should alter model-based predictions of injury. Therefore, incorporating this heterogeneity may be important for increasing the accuracy of computational predictions of sports-related concussion and other forms of mild TBI. Further studies of the microstructure of the pia-arachnoid complex are needed to fully characterize the link between microstructural constituents and microstructure properties such as tethering stiffness.

Acknowledgements

The authors would like to acknowledge the financial support of *NSF Smart and Connected Health Award No. 1622741*.

References

Alhilali, L. M. *et al.* (2015) 'Biomechanical characterization of human dura mater', *Stapp Car Crash J.* 2011/12/22. New York: Taylor & Francis, 16(1), pp. 441–454. doi: 10.1148/radiol.2015142974.

Cloots, R. J. H. *et al.* (2008) 'Biomechanics of traumatic brain injury: Influences of the morphologic heterogeneities of the cerebral cortex', *Ann Biomed Eng*. 2008/05/10, 36(7), pp. 1203–1215. doi: 10.1007/s10439-008-9510-3.

Cloots, R. J. H. *et al.* (2011) 'Micromechanics of diffuse axonal injury: Influence of axonal orientation and anisotropy', *Biomech Model Mechanobiol*. 2010/07/17, 10(3), pp. 413–422. doi: 10.1007/s10237-010-0243-5.

Cloots, R. J. H. *et al.* (2013) 'Multi-scale mechanics of traumatic brain injury: Predicting axonal strains from head loads', *Biomech Model Mechanobiol*. 2012/03/22, 12(1), pp. 137–150. doi: 10.1007/s10237-012-0387-6.

Cloots, R. J. H., van Dommelen, J. A. W. and Geers, M. G. D. (2012) 'A tissue-level anisotropic criterion for brain injury based on microstructural axonal deformation', *J Mech Behav Biomed Mater*. 2011/11/22, 5(1), pp. 41–52. doi: 10.1016/j.jmbbm.2011.09.012.

Coats, B. and Margulies, S. S. (2006) 'Material properties of human infant skull and suture at high rates', *Journal of Neurotrauma*. doi: 10.1089/neu.2006.23.1222.

Coronado, V. G. *et al.* (2012) 'Trends in traumatic brain injury in the U.S. and the public health response: 1995-2009', *Journal of Safety Research*, 43(4), pp. 299–307. doi: 10.1016/j.jsr.2012.08.011.

Fabris, G., Suar, Z. M. and Kurt, M. (2019) 'Micromechanical heterogeneity of the rat pia-arachnoid complex', *Acta Biomaterialia*. doi: 10.1016/j.actbio.2019.09.044.

Ghaffari, M. *et al.* (2014) 'Fluid Structure Interaction of Traumatic Brain Injury: Effects of Material Properties on SAS Trabeculae', *International Journal of Modern Engineering*, 14(2), pp. 54–62.

Ghajari M., Hellyer P.J., and Sharp D.J. (2017) 'Computational modelling of traumatic brai ninjury preditcts the locaiton of chronic traumatic encephalopathy pathology', *Brain*, 140(2), pp. 333-343. doi: 10.1093/brain/aww317

Giannini *et al.* (2008) 'Effects of freezing on the biomechanical and structural properties of human posterior tibial tendons', *Int Orthop*, 32(2), pp. 145-151. doi: 10.1007/s00264-006-0297-2

Haines, D. E. (1991) 'On the question of a subdural space', *The Anatomical Record*, 230(1), pp. 3–21. doi: 10.1002/ar.1092300103.

Haines, D. E. and Ard, M. D. (2002) *Fundamental neuroscience*. 2nd edn. New York: Churchill Livingstone.

Ji, S. *et al.* (2015) 'Group-wise evaluation and comparison of white matter fiber strain and maximum principal strain in sports-related concussion', *J Neurotrauma*, 32(7), pp. 441–454. doi: 10.1089/neu.2013.3268.

Jin, X. *et al.* (2006) 'Biomechanical response of the bovine pia-arachnoid complex to tensile loading at varying strain-rates', *Stapp Car Crash J*. 2007/02/22, 50, pp. 637–649. doi: 10.4271/2006-22-0025.

Jin, X. *et al.* (2007) 'Biomechanical response of the bovine pia-arachnoid complex to normal traction loading at varying strain rates', *Stapp Car Crash J*. 2008/02/19, 51, pp. 115–126. Available at: https://www.ncbi.nlm.nih.gov/pubmed/18278593.

Jin, X. *et al.* (2014) 'Constitutive modeling of pia-arachnoid complex', *Ann Biomed Eng*. 2013/12/11, 42(4), pp. 812–821. doi: 10.1007/s10439-013-0948-6.

Jin, X., Yang, K. H. and King, A. I. (2011) 'Mechanical properties of bovine pia-arachnoid complex in shear', *J Biomech*. 2010/11/23, 44(3), pp. 467–474. doi: 10.1016/j.jbiomech.2010.09.035.

De Kegel, D. *et al.* (2018) 'Biomechanical characterization of human dura mater', *Journal of the Mechanical Behavior of Biomedical Materials*, 79, pp. 122–134. doi: https://doi.org/10.1016/j.jmbbm.2017.12.023.

Kleiven S. (2006) 'Evaluation of head injury criteria using a finite element model validated against experiments on localized brain motion, intracerebral acceleration, and intracranial pressure', *International Journal of Crashworthiness*, 11(2), pp. 65-79. doi: 10.1533/ijcr.2005.0384

Kuijpers, A. H., Claessens, M. H. and Sauren, A. A. (1995) 'The influence of different boundary conditions on the response of the head to impact: a two-dimensional finite element study', *J Neurotrauma*. 1995/08/01, 12(4), pp. 715–724. doi: 10.1089/neu.1995.12.715.

Langlois, J. A., Rutland-Brown, W. and Wald, M. M. (2006) 'The epidemiology and impact of traumatic brain injury: A brief overview', *Journal of Head Trauma Rehabilitation*. 2006/09/20, 21(5), pp. 375–378. doi: 10.1097/00001199-200609000-00001.

Lee, A.H. and Elliott, D.M. (2017) 'Freezing does not alter multiscale tendon mechanics and damage mechanisms in tension', *Ann NY Acad Sci*, 1409(1), pp. 85-94. doi: 10.1111/nyas.13460

Mao, H. *et al.* (2013) 'Development of a finite element human head model partially validated with thirty five experimental cases', *Journal of Biomechanical Engineering*, 135(11). doi: 10.1115/1.4025101.

Margulies, S. and Coats, B. (2013) ‘Experimental Injury Biomechanics of the Pediatric Head and Brain’, in *Pediatric Injury Biomechanics*. doi: 10.1007/978-1-4614-4154-0_4.

Patton, D. A., McIntosh, A. S. and Kleiven, S. (2013) ‘The biomechanical determinants of concussion: finite element simulations to investigate brain tissue deformations during sporting impacts to the unprotected head’, *J Appl Biomech*. 2013/02/26, 29(6), pp. 721–730. Available at: https://www.ncbi.nlm.nih.gov/pubmed/23434739.

Prange, M. and Meaney, D. F. (2000) ‘Defining Brain Mechanical Properties: Effects of Region, Direction, and Species’, in *SAE Technical Papers*. doi: 10.4271/2000-01-SC15.

Saboori, P. and Sadegh, A. (2011) ‘Material modeling of the head’s subarachnoid space’, *Scientia Iranica*. doi: 10.1016/j.scient.2011.11.032.

Scott, G. G. and Coats, B. (2015) ‘Microstructural Characterization of the Pia-Arachnoid Complex Using Optical Coherence Tomography’, *IEEE Transactions on Medical Imaging*. 2015/02/03, 34(7), pp. 1452–1459. doi: 10.1109/TMI.2015.2396527.

Scott, G. G., Margulies, S. S. and Coats, B. (2016) ‘Utilizing multiple scale models to improve predictions of extra-axial hemorrhage in the immature piglet’, *Biomechanics and Modeling in Mechanobiology*. 2015/11/21, 15(5), pp. 1101–1119. doi: 10.1007/s10237-015-0747-0.

Szarko, M., Muldrew, K., and Bertram, J.E.A. (2010) 'Freeze-thaw treatment effects on the dynamic mechanical properties of articular cartilage', *BMC Musculoskelet Disord*, 11(231). doi: 10.1186/1471-2474-11-231,

Takhounts, E.G. *et al.* (2008) 'Investigation of traumatic brain injuries using the next generaiton of simulated injury monitor (SIMon) finite element head model.', *Stapp Car Crash Journal*, 52, pp.1-31.

Yin, Z. *et al.* (2018) ‘In vivo Characterization of 3D Skull and Brain Motion During Dynamic Head Vibration Using Magnetic Resonance Elastography HHS Public Access’, *Magn Reson Med*, 80(6), pp. 2573–2585. doi: 10.1002/mrm.27347.

Zhao, Wei; Stemper, B. and Ji, S. (2019) ‘A STUDY OF THE BRAIN-SKULL INTERFACE CONDITIONS OF THE WORCESTER RAT HEAD INJURUY MODEL (WRHIM)’, in *Summer Biomechanics, Bioengineering and Biotransport Conference*. Seven Springs, pp. 528–529.

Zhao, W., Choate, B. and Ji, S. (2018) ‘Material properties of the brain in injury-relevant conditions – Experiments and computational modeling’, *Journal of the Mechanical Behavior of Biomedical Materials*, 80, pp. 222–234. doi: 10.1016/j.jmbbm.2018.02.005.

Zhou, Z., Li, X. and Kleiven, S. (2019) ‘Fluid–structure interaction simulation of the brain–skull interface for acute subdural haematoma prediction’, *Biomechanics and Modeling in Mechanobiology*, 18(1), pp. 155–173. doi: 10.1007/s10237-018-1074-z.

Figures Legends

Fig. 1: (A) Positioning of OCT lens and pressurization system in brain. (B) Schematic of inflation system used to pressurize the subarachnoid space. (C) Example of a 3D volumetric OCT scan used for measuring microstructure contents.

Fig 2: Time series of subarachnoid space inflation show displacement of arachnoid membrane and stretching of arachnoid trabeculae under hydrostatic pressure.

Fig. 3: Stress-strain plots for the three inflation regimes found within one subject. During inflation, arachnoid trabeculae either unfolded during the inflation, were fully recruited during the inflation, or were a combination of the two behaviors. Only fully recruited regimes were used for statistical analysis.

Fig. 4: Stress-strain data from all fully recruited trabeculae tests.

Fig. 5: Data comparing modulus (E), arachnoid trabeculae volume fraction (ATVF), vessel volume fraction (VVF), and arachnoid membrane thickness (AMT) in 5 different subjects. Symbols indicate significant differences between subject measures. Error bars indicate standard deviation.

Fig. 6: Data comparing modulus (E), arachnoid trabeculae volume fraction (ATVF), vessel volume fraction (VVF), and arachnoid membrane thickness (AMT) in 6 different regions of the brain. * Indicates significant differences between region measures. Error bars indicate standard deviation. No error bars are presented for VVF because data were not normally distributed.

Fig 7: Voronoi tessellation map of modulus measurements demonstrate higher modulus in superior regions of the brain. The Voronoi polygons are constructing by using each scan location as a seed point, and creating perpendicular bisectors between each neighboring seed point. Dotted lines indicate superior/inferior and frontal/parietal/occipital boundaries.

Tables

Table 1: Post-mortem human cadaver information

Subject	Sex	Age (yrs.)
#1	Male	81
#2	Male	70
#3	Male	50
#4	Female	32
#5	Female	67

Table 2: Modulus data by regional group and subject for tests selected for microstructure comparisons. Tests grouped by anatomical region were computed using matched pairs analysis to isolate subject and region effects. Bold font indicates statistical significance.

Data Grouping	Modulus (kPa)			
	n	Mean	STD	*p*-value
Frontal	11	10.9	4.7	
Parietal	16	11.1	4.7	0.36
Occipital	9	13.8	4.7	
Inferior	17	10.4	4.2	**0.0224**
Superior	19	12.9	4.9	
Left	19	11.6	5.2	0.765
Right	17	11.7	4.2	
Subject 1	8	11.7	5.8	
Subject 2	10	8.9	3.9	
Subject 3	8	12	3.3	0.1347
Subject 4	6	15.1	3.5	
Subject 5	4	12.6	6.3	

Fig. 1

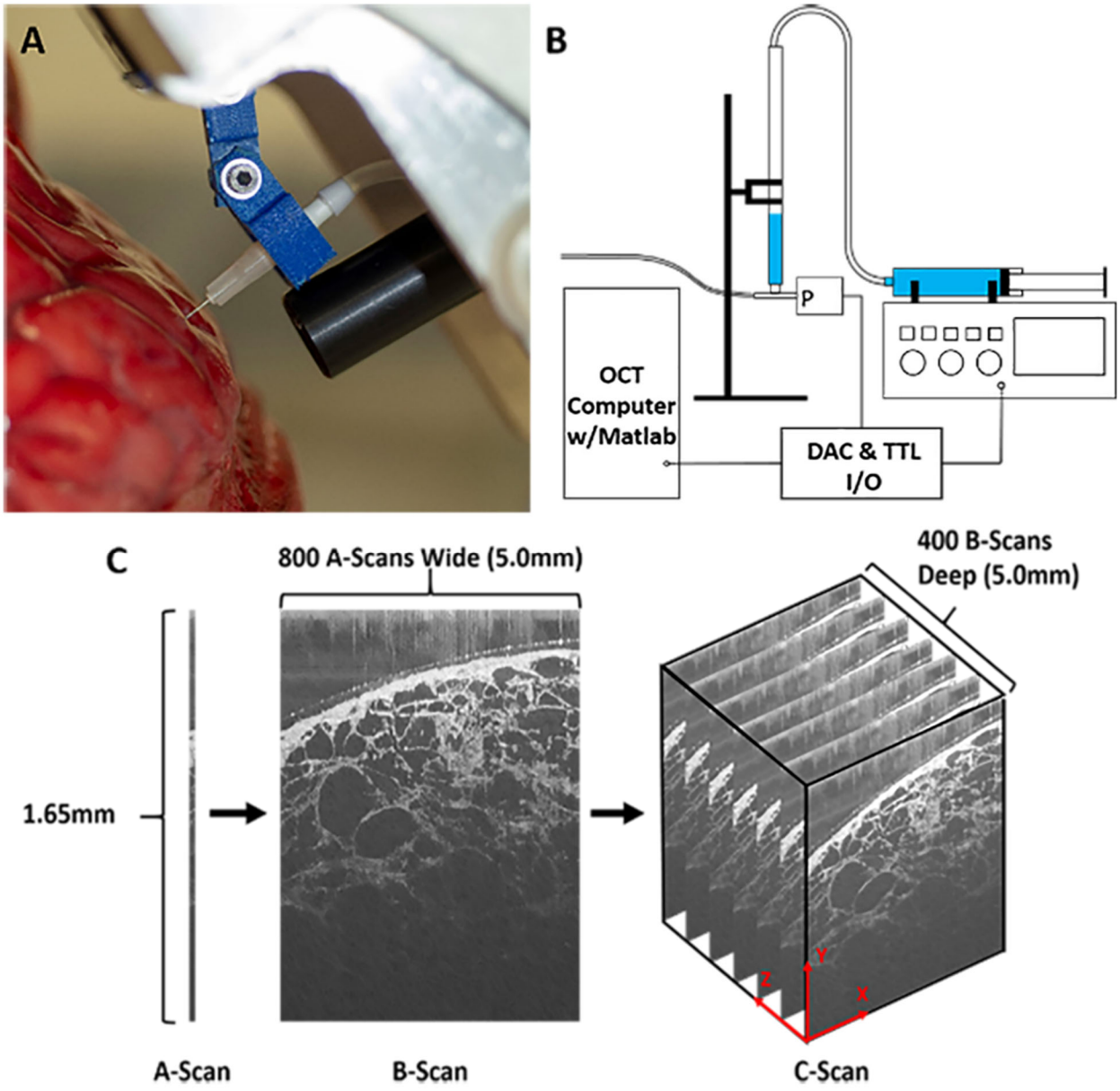
A
B
P
OCT
Computer
w/Matlab
DAC & TTL
I/O
C
800 A-Scans Wide (5.0mm)
400 B-Scans
Deep (5.0mm)
1.65mm
Y
Z
X
A-Scan
B-Scan
C-Scan

Fig 2.

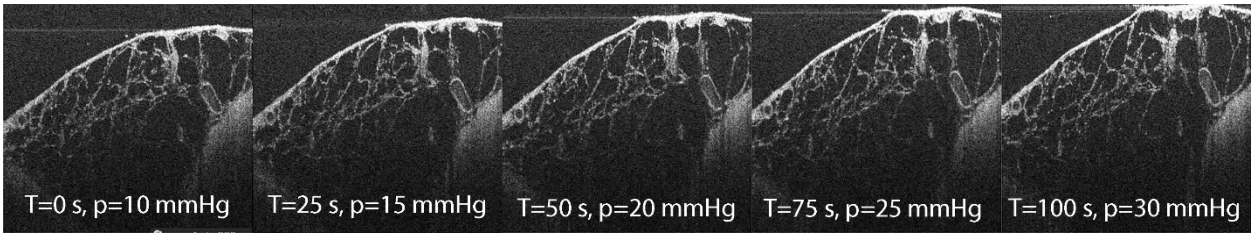
T=0 s, p=10 mmHg
T=25 s, p=15 mmHg
T=50 s, p=20 mmHg
T=75 s, p=25 mmHg
T=100 s, p=30 mmHg

Fig. 3

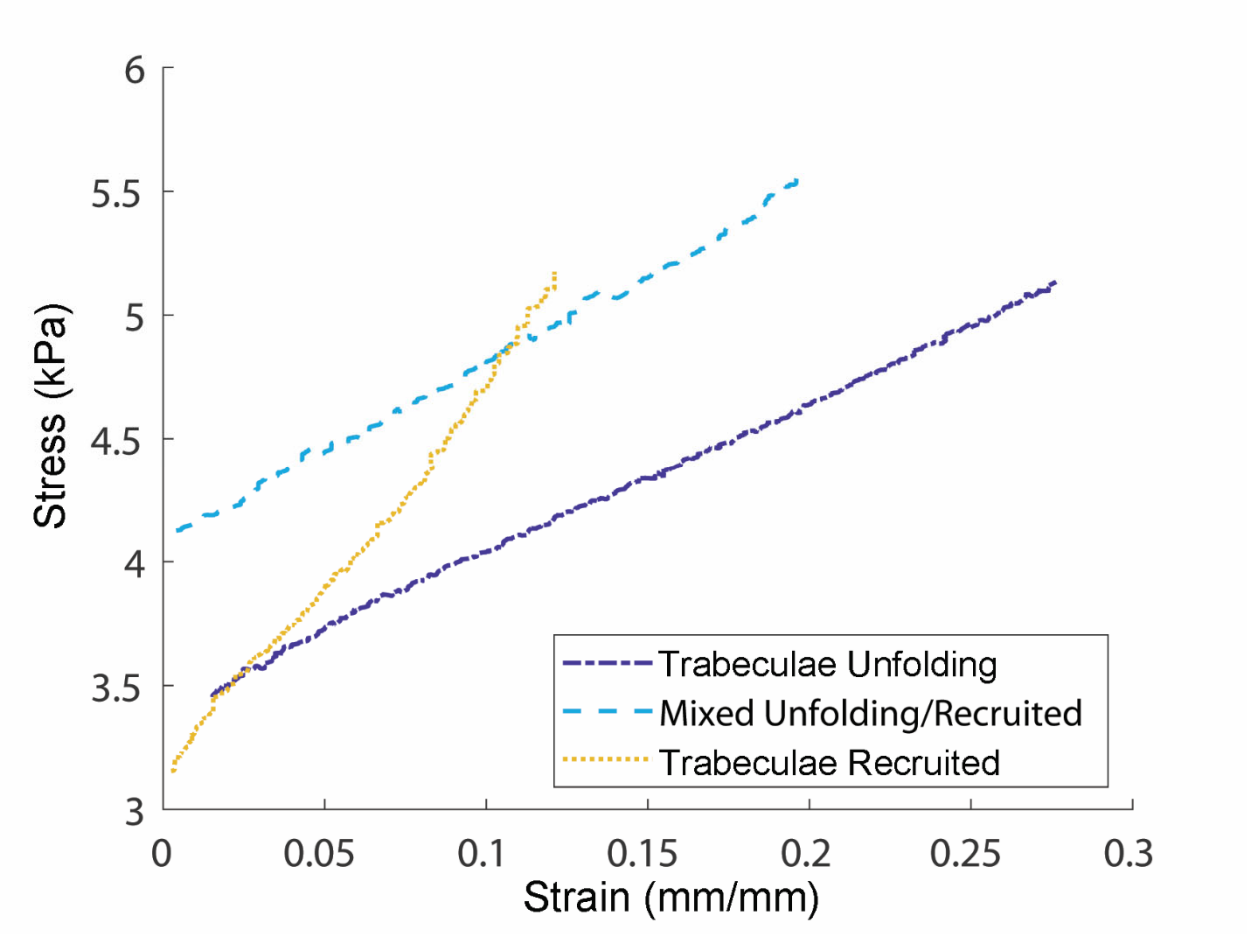
6
5.5
5
4.5
4
3.5
3
Stress (kPa)
0
0.05
0.1
0.15
0.2
0.25
0.3
Strain (mm/mm)
Trabeculae Unfolding
Mixed Unfolding/Recruited
Trabeculae Recruited

Fig. 4

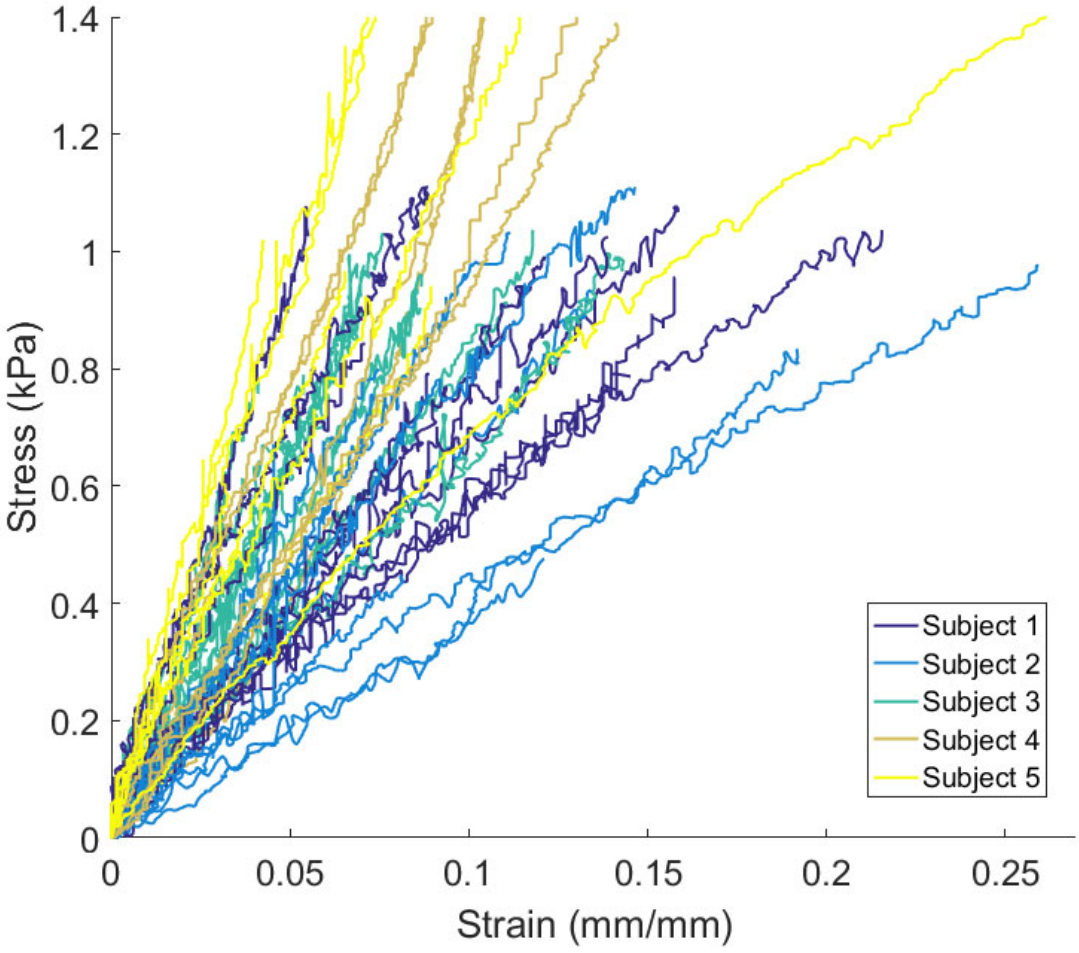
1.4
1.2
1
0.8
0.6
0.4
0.2
0
Stress (kPa)
0
0.05
0.1
0.15
0.2
0.25
Strain (mm/mm)
Subject 1
Subject 2
Subject 3
Subject 4
Subject 5

Fig. 5

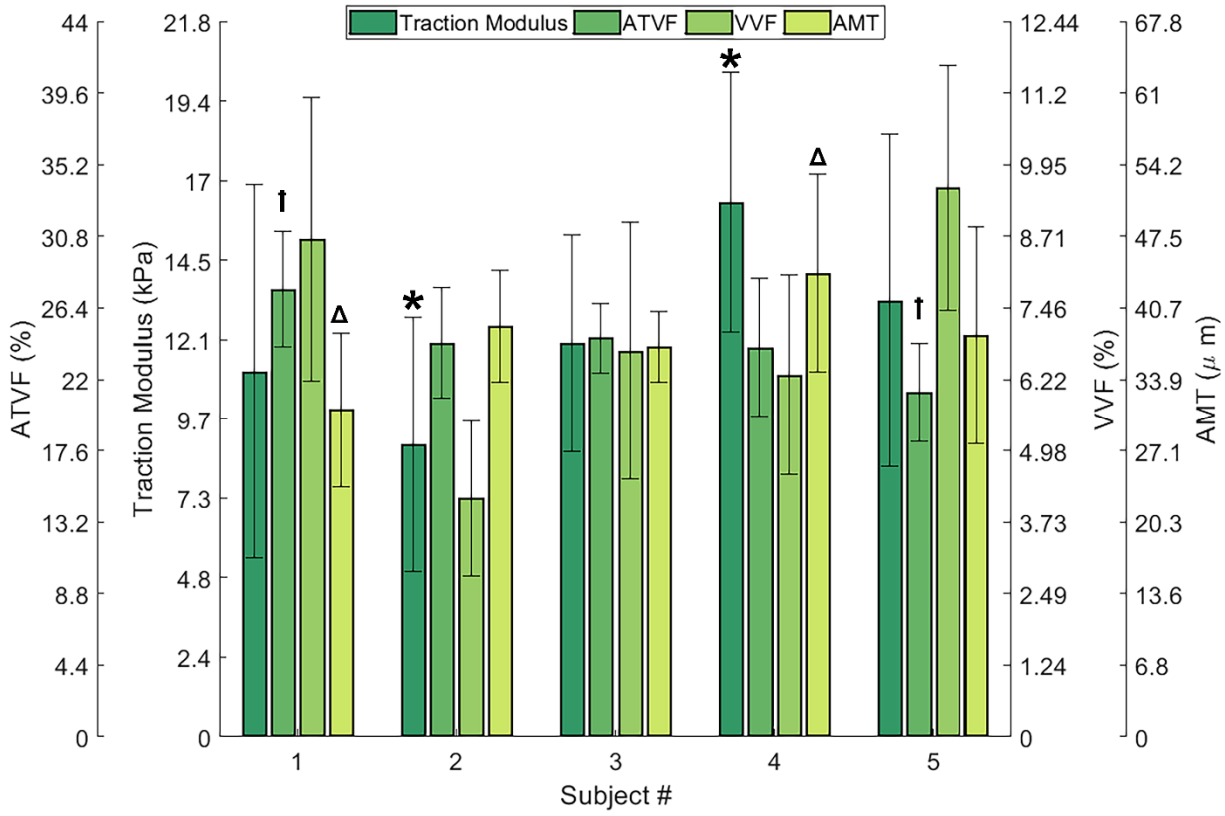
Traction Modulus
ATVF
VVF
AMT
ATVF (%)
Traction Modulus (kPa)
VVF (%)
AMT (μ m)
Subject #
1
2
3
4
5
*
†
Δ

Fig. 6

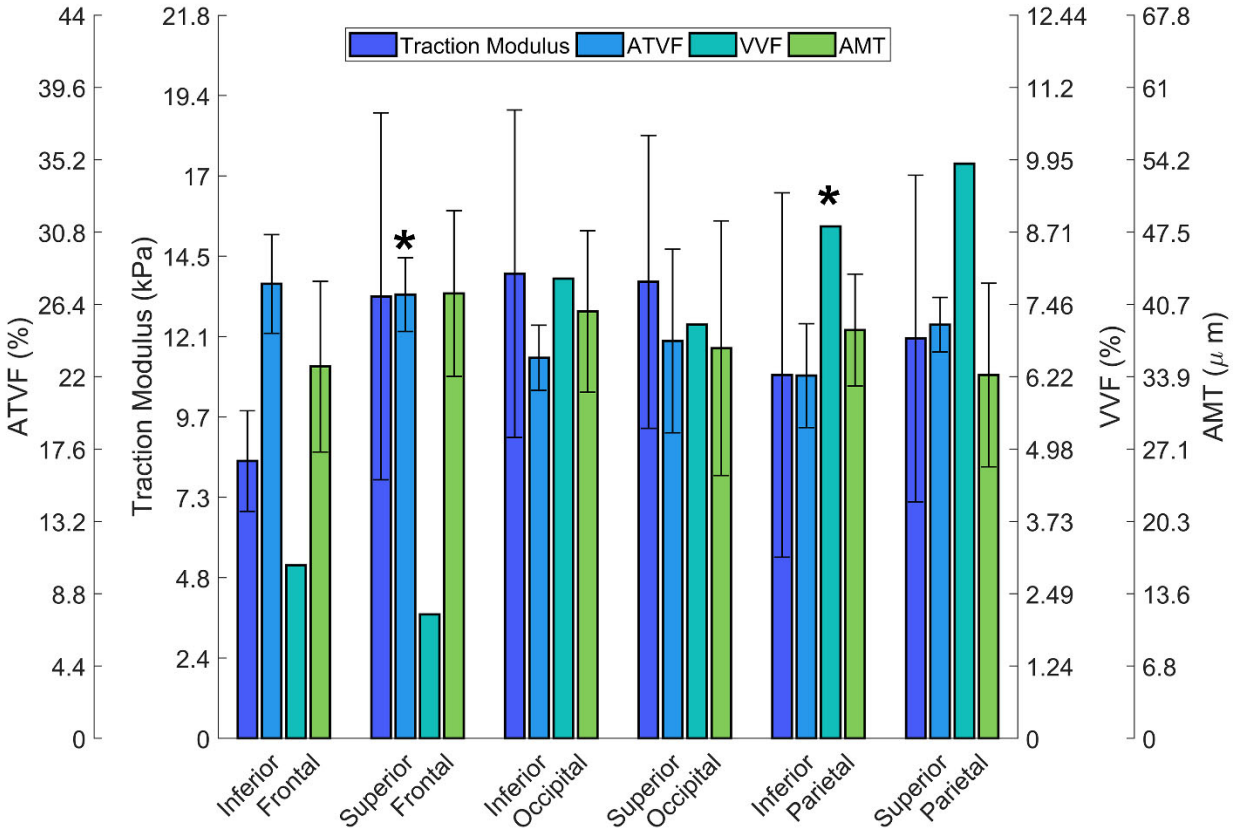
Traction Modulus
ATVF
VVF
AMT
ATVF (%)
Traction Modulus (kPa)
VVF (%)
AMT (μ m)
44
39.6
35.2
30.8
26.4
22
17.6
13.2
8.8
4.4
0
21.8
19.4
17
14.5
12.1
9.7
7.3
4.8
2.4
0
12.44
11.2
9.95
8.71
7.46
6.22
4.98
3.73
2.49
1.24
0
67.8
61
54.2
47.5
40.7
33.9
27.1
20.3
13.6
6.8
0
*
*
Inferior Frontal
Superior Frontal
Inferior Occipital
Superior Occipital
Inferior Parietal
Superior Parietal

Fig. 7